Carbon 179 (2021) 514–522

Contents lists available at ScienceDirect

Carbon

journal homepage: www.elsevier.com/locate/carbon

Research Article

NH_2 linker for femtomolar label-free detection with reduced graphene oxide screen-printed electrodes

Jagriti Sethi [a, *], Ahmed Suhail [a, b], Mina Safarzadeh [a], Anas Sattar [c], Yinghui Wei [d], Genhua Pan [a]

[a] Wolfson Nanomaterials and Devices Laboratory, School of Engineering, Computing and Mathematics, University of Plymouth, Devon, PL4 8AA, UK
[b] College of Science, Department of Physics, University of Mosul, Mosul, Iraq
[c] School of Biomedical and Healthcare Sciences, Peninsula Schools of Medicine and Dentistry, University of Plymouth, Devon, PL4 8AA, UK
[d] School of Engineering, Computing and Mathematics, University of Plymouth, Devon, PL4 8AA, UK

ARTICLE INFO

Article history:
Received 10 January 2021
Received in revised form
22 April 2021
Accepted 23 April 2021
Available online 26 April 2021

Keywords:
NH_2 linker
Reduced graphene oxide
Label-free
Electrochemical biosensors
Beta-amyloid
Alzheimer's disease

ABSTRACT

Surface modification with linker molecules is necessary for the effective immobilization of bioreceptors and for improving the performance of biosensors. In this work, we present a novel functionalization technique to attach amine (NH_2) linker on graphene-based sensor surfaces. This is achieved by reacting the commercially available reduced graphene oxide (rGO) screen-printed electrodes (SPEs) with ammonia solution at room temperature. The NH_2 linkers are attached predominantly on the edge and defect sites of rGO SPE through chemisorption as shown by XPS, Raman and FTIR analysis. The functionalized SPEs are further characterized using morphological and electrochemical techniques. The validation of the linker is done by using the functionalized SPEs for the detection of $A\beta_{1\text{-}40}$ and $A\beta_{1\text{-}42}$ biomarkers. A limit of detection (LOD) of 9.51 fM is achieved over a linear dynamic range of 10 fM-10 pM for $A\beta_{1\text{-}40}$. Similarly, LOD of 8.65 fM is achieved over a linear dynamic range of 10 fM-50 pM for $A\beta_{1\text{-}42}$. This excellent sensitivity is attributed to the functionalization of rGO surface with NH_2 linker, which provides a large number of binding sites for bioreceptors. High specificity for the target biomarkers over interfering Aβ and ApoE ε4 species is also demonstrated. The biosensor is further validated for the analysis of spiked human plasma. The proposed technique provides a promising approach for improving the detection sensitivity of graphene biosensors for application in biofluids based minimally invasive and cost- and time-efficient disease diagnosis.

1. Introduction

In recent years, there has been an increasing demand for rapid, sensitive, minimally invasive, and reliable diagnostic platforms to facilitate the monitoring of chronic diseases [1,2]. This has led to extensive research in the field of biosensors because of their ability to detect biomarkers in a cost- and time-efficient manner [3,4]. Biosensors are analytical devices consisting of specific bioreceptors to interact with biological samples and transducers to convert these interactions into quantifiable data [5,6]. The immobilization of bioreceptors on the sensor surfaces is a crucial step, which directly influences the sensing performance and is often achieved through specific linker chemistry [3,7]. Linker conjugation with nanomaterials such as graphene and reduced graphene oxide (rGO) has been shown to improve the performance of biosensors [8–10]. This is attributed to their high conductivity [11], large surface-to-volume ratio [12] and ease of surface functionalization [10,13] of graphene surfaces. Consequently, several graphene platforms based on different linker chemistries have been developed for the detection of various disease biomarkers [9,14–16]. However, insufficient sensitivity and non-specific bindings are major drawbacks, which limit their clinical applications [17]. Moreover, the multiple surface modification steps prior to immobilization of bio receptors often complicates the fabrication process and increase the overall cost [18,19].

Recently, a paper-based graphene biosensor with electro polymerized aniline (PANI) layer was developed for the detection of human interferon-gamma (IFN-γ), a biomarker for tuberculosis [20]. PANI was used for signal amplification and linking the antibody on the graphene surface. The amine groups of PANI were

* Corresponding author.
E-mail address: jagriti.sethi@plymouth.ac.uk (J. Sethi).

https://doi.org/10.1016/j.carbon.2021.04.074

activated with a commonly used 1-ethyl-3-(3-dimethylaminopropyl) carbodiimide hydrochloride (EDC) - *N*-hydroxysuccinimide (NHS) coupling chemistry. EDC is a zero-length cross linker, which is reactive towards the carboxyl and amine groups, while NHS is a reagent that stabilizes the intermediates formed during the two-step conjugation [21]. Although, the biosensor has limit of detection (LOD) in picomolar (pM) range, multiple surface modification steps increased the complexity of the fabrication process. Another biosensor based on carboxyl-enriched porous carbon/graphene electrode used EDC-NHS chemistry for the detection of engrailed-2 (EN2), a prostate cancer biomarker [17]. The LOD of the biosensor was found in the nanomolar (nM) range, which is inadequate for clinical diagnostics of EN2. Moreover, the biosensor failed to show applicability in the real bio fluidic samples. Our previous work [10] investigated the use of pyrenebutyric acid *N*-hydroxysuccinimide ester (Pyr-NHS) linker for improving the performance of biosensors. The modification of graphene/rGO dual-layer with Pyr-NHS provided a specific and reliable tool for the detection of $A\beta_{1\text{-}42}$, an Alzheimer's disease (AD) biomarker, from plasma samples [10]. Linker chemistry was based on the non-covalent attachment of Pyr-NHS on the rGO surface without adversely affecting its structure [22]. Pyr-NHS has also been successfully used for developing a sensitive and reliable biosensor for the detection of Clusterin, another AD biomarker [22,23]. However, the LOD of these biosensors was found in pM ranges, which is insufficient in identifying different stages of AD [24,25] and/or detect certain biomarkers in the early stages [26]. The higher LOD is attributed to the bulkiness of the Pyr-NHS group, which contains one functional group per molecule and thus, provides less number of binding sites for bioreceptors [27].

The direct approach of attaching primary amines (NH_2) on the sensor surface has shown potential for the effective immobilization of bioreceptors [28]. Unlike Pyr-NHS, the NH_2 molecule is small and therefore attaches on the surface in higher numbers to provide large number of binding sites [29]. This increases the probability of attaching a higher number of bioreceptors to capture the target biomarker. However, the functionalization process is usually based on complex reactions, which are time consuming and involves complicated instruments [28–30].

In this work, a novel technique for the functionalization with NH_2 linker has been developed using commercially available rGO screen-printed electrode (SPEs). XPS, Raman and FTIR analysis show that functionalization chemistry is based on the chemisorption of NH_2 linker predominantly on the defect and edge sites of rGO without damaging its structure [31–33]. Femtomolar (fM) detection and high specificity were demonstrated for $A\beta_{1\text{-}40}$ and $A\beta_{1\text{-}42}$ biomarkers of AD. The biosensors are further validated with human plasma spiked with different $A\beta_{1\text{-}40}$ and $A\beta_{1\text{-}42}$ concentrations to confirm its reliability for biofluidic analysis.

2. Experimental section

2.1. Reagents

Ammonium hydroxide solution/ammonia solution (ACS reagent, 28–30% NH_3 basis), phosphate buffered saline (PBS), potassium ferricyanide (K3Fe(CN)6), potassium chloride (KCl), bovine serum albumin (BSA), Eppendorf® LoBind microcentrifuge tubes, human $A\beta_{1\text{-}42}$ peptides and human plasma were purchased from Sigma Aldrich (Dorset, UK). $A\beta_{1\text{-}40}$ and ApoE ε4 peptides were obtained from Tocris (UK). $A\beta_{1\text{-}40}$ antibody was obtained from Biolegend, UK. Pierce™ recombinant protein G and $A\beta_{1\text{-}42}$ antibody (H31L21) were purchased from Thermo Fisher Scientific (USA).

2.2. Apparatus

The rGO-modified SPEs and μstat ECL potentiostat were purchased from Metrohm Dropsens (UK). Differential pulse voltammetry (DPV) and cyclic voltammetry (CV) measurements were performed at room temperature using a μstat ECL potentiostat and controlled by DropView 8400 2.0 software.

Raman spectroscopy of the electrode was carried out using a XPLORA HORIBA system with a 532 nm laser source, scan range of 1100–2000 cm^{-1}, a 100*x* objective lens with a power of 100 mW, and an exposure time of 5–60 s. Thermo Scientific™ Nexsa™ system was used for performing the X-ray photoelectron spectroscopy (XPS) analysis with a monochromatic X-ray source (1486.68 eV). For the wide scan, pass energy was 200 eV with a step size of 1 eV and 10 scans. For the high-resolution scan, pass energy was 40 eV with a step size of 0.1 eV and 20 scans. Morphological characterization was performed with JEOL 6610 LV scanning electron microscope (SEM) from Oxford Instruments of 30 kV.

2.3. Electrochemical measurements

The measurements were performed with an electrolyte solution of 10 mM potassium ferricyanide solution and 1 M KCl solution as the supporting electrolyte. CV was acquired at the scan rate of 50 mV s^{-1} from −0.2 to 0.5 V without applying any preconditioning potential or accumulation time. The data were acquired at the working potential of ~310 mV. DPV was recorded from −0.15 V to +0.45 V at the scan rate of 50 mV s^{-1}, pulse amplitude of 50 mV, step potential of 10 mV and pulse period of 0.4 s. The data were acquired at the working potential of ~165 mV.

2.4. Fabrication of biosensor

First, rGO SPEs were immersed in ammonia solution (containing 28–30% NH_3) for 30 min at room temperature referred to as ammonia treatment [62]. After that, the electrodes were gently dried with nitrogen and kept in vacuum until further use. The $A\beta_{1\text{-}42}$ antibody solution (20 μg/mL) was mixed in the ratio of 70:30 with protein G (20 μg/mL) using a vortex mixer. This mixture was kept at room temperature for 30 min to enable strong bond formation. The $A\beta_{1\text{-}40}$ antibody (20 μg/mL) and protein G (20 μg/mL) mixture was prepared in the same ratio (70:30). Then, ammonia-treated SPEs were incubated in the antibody and protein G mixture for 6 h at room temperature. Subsequently, the SPEs were washed with PBS buffer for removing any unbound antibodies. Finally, 1% BSA (in PBS) was drop casted onto the SPEs for 15 min followed by rinsing with PBS. All the incubation time periods were optimised to achieve the highest sensitivity for the proposed biosensor (Supplementary information, Fig. S3).

2.5. Interaction of biomarkers with the sensor

The desired dilutions of $A\beta_{1\text{-}40}$ and $A\beta_{1\text{-}42}$ peptides were freshly prepared in PBS by vortex mixing for 20 s. The prepared peptides were kept on ice during the experiments. Next, 10 μL of each peptide solution was drop casted on the biosensor and incubated at room temperature for 1 h. The sensor was then rinsed with PBS to remove any unbound peptides. The measurement time for each sensor is approximately 3–4 min.

2.6. Spiked sample analysis

Human plasma was diluted with PBS in the ratio of 1:100. The desired dilutions of the two biomarkers were prepared in plasma by vortex mixing for 20 s. The biosensors were then incubated with

spiked samples for 60 min followed by washing with PBS and measurement.

3. Results and discussion

3.1. XPS analysis

XPS analysis was performed to estimate the chemical states and atomic ratio of bare rGO (black) and ammonia-treated rGO (red). The wide region spectra of both surfaces show carbon (C) (~284 eV), nitrogen (N) (~400 eV) and oxygen (O) (~532 eV) peaks (Fig. 1(a)). The presence of N peak in bare rGO can be attributed to the chemicals involved in the reduction of graphene oxide [9]. The atomic percentage (at%) of the samples were calculated using the CasaXPS software. After the ammonia treatment, the at% of N increases from 0.6 to 1.2, which indicates the adsorption of *N*-containing functional groups on the surface of rGO [34]. Additionally, at% of C and O species for bare and ammonia-treated rGO was also calculated as shown in Table S1. To further confirm the adsorption of NH_3 or NH_2, the nature of C and N species was analysed. The C1s high resolution spectra of ammonia-treated rGO (Fig. 1 (b)) demonstrate three peaks emerging from C–C/C=C in aromatic rings (~284.5 eV), C–O/C–N (~286.6 eV) and O–C=O (~288.6 eV) bonds [9,35,36]. The C–N peaks appear at the same ranges as C–O, which is the reason for a significant increase in the peak at ~286.6 eV as compared to bare rGO electrode [37–41]. The N1s high resolution spectra, as shown in Fig. 1 (c), can be deconvoluted into two peaks, namely C–N (~400 eV) from amines (NH_2) and C–N^+ (~402 eV) from quaternary nitrogen [34]. After the treatment, the peak height of C–N doubled while no significant

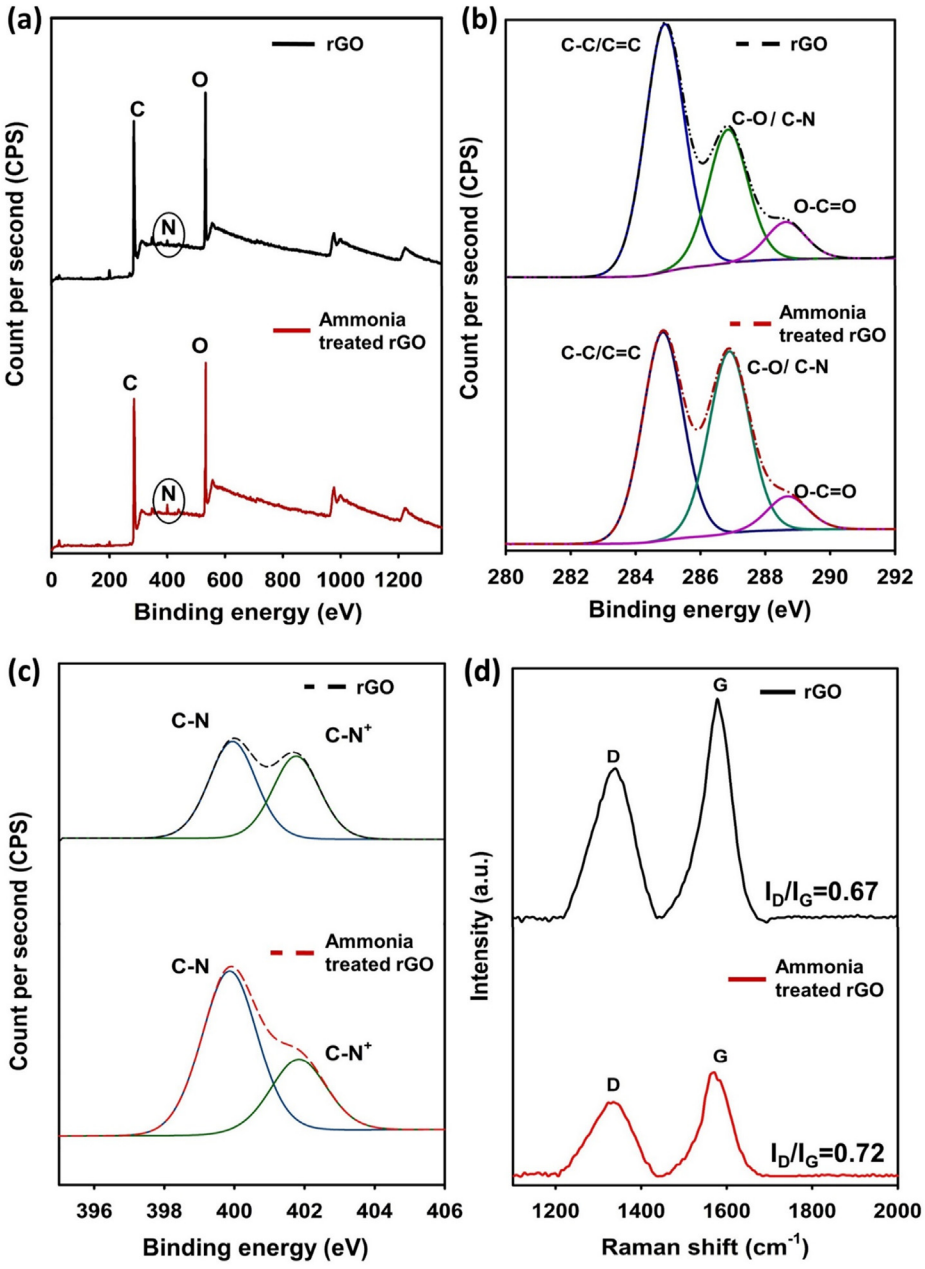

Fig. 1. Spectral analysis of the SPE before and after the ammonia treatment (a) overall scan; (b) C1s scan; (c) N1s scan and (d) Raman Spectra. (A colour version of this figure can be viewed online.)

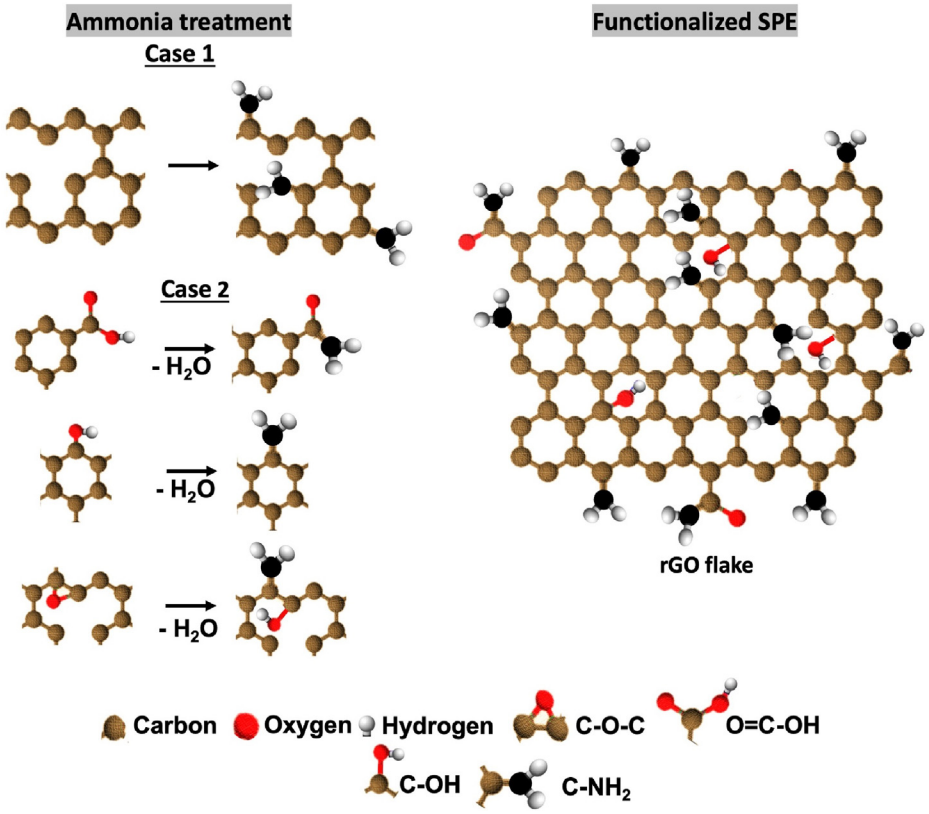

Fig. 2. Chemisorption-based reaction mechanism proposed for the NH_2 functionalization of rGO SPE. (A colour version of this figure can be viewed online.)

shift was observed in the C–N^+ peak as compared to that of bare rGO [34,42]. These results indicate that the ammonia treatment leads to loading of NH_2 molecules on the rGO surface through chemisorption.

3.2. Raman analysis

Raman spectra of rGO and ammonia-treated rGO is shown in Fig. 1 (d) with signature D and G bands. D band represents the out-of-plane vibrations in disordered structures whereas G band is associated with in-plane vibrations of ordered sp^2 C atoms in the graphitic structures [43]. Ratio of the intensity of D to G band (I_D/I_G) illustrates the structural defect in rGO lattice [9]. After the ammonia treatment, D band remains at ~1340 cm^{-1}, however, a slight shift in the G band from ~1580 cm^{-1} to ~1575 cm^{-1} is observed. Similar shifts have been observed in the literature for amine functionalized graphene materials [44,45]. Further, I_D/I_G increases from 0.67 for bare rGO to 0.72 for ammonia-treated rGO. This suggests that chemisorption of NH_2 introduces some defects in rGO lattice due to the chemical bonding, which leads to an increase in sp^3 planar carbon atoms [44,46]. However, the increase is not significant, which confirms that no major defects were introduced into the rGO structure. This indicates that NH_2 groups are attached on the available active sites on rGO without affecting its honeycomb lattice. In addition, slight increase is also observed in full width at half maximum (FWHM) for ammonia-treated rGO. These changes confirm the successful attachment of amine groups on the rGO surface [44,47,48].

3.3. Reaction mechanism

Surface chemistry of rGO functionalization is proposed based on the XPS, Raman and FTIR analysis (Supplementary information, Fig. S2). The reaction of ammonia solution ($NH_3 \cdot H_2O$) with rGO can occur either by chemisorption of NH_2 groups on the edge/defect sites and oxygen functionalities as shown in Fig. 2 [31] or by replacement of carbon (C) atoms in the lattice with nitrogen (N) atom [47]. However, the latter is not possible without the application of high temperature and pressure [47] and can lead to changes in the electronic properties of rGO affecting its sensing performance [7]. Therefore, chemisorption of NH_2 is the only possibility for the present study, which can occur in one of the following ways:

Case 1. NH_2/ defect sites or carbon vacancy: This is the most plausible mechanism as rGO flakes have many vacant/ defect sites, particularly around the edges [49]. There are many available sites for the attachment of NH_2 as the electrode is made of stacks of rGO flakes. The NH_3/NH_4^+ present in ammonia solution can interact with C atoms resulting in adjacent C–NH_2 and C–H bonds (Fig. 2) [32,50]. The defect sites create a state of non-equilibrium in the structural network and therefore readily bond with NH_2 to stabilize it [33]. This is a common phenomenon observed in case of CNTs where the defect site chemistry has been quite useful for attachment of functional groups on the surface [51]. The successful functionalization of the rGO surface is confirmed with C1s and N1s high resolution spectra (Fig. 1 (b, c)) that depicts an increase in the intensity of C–N peak from amines at ~286.6 eV and ~400 eV respectively. Raman spectra (Fig. 1 (d)) depicts that no major defects were introduced during the functionalization process, which further confirms that the chemisorption does not adversely affect the honeycomb structure of rGO. Further, FTIR analysis (Fig. S2) shows the peaks at 3371, 1100 and 1066 cm^{-1} exhibiting *N*–H stretch vibrations and C–N stretch.

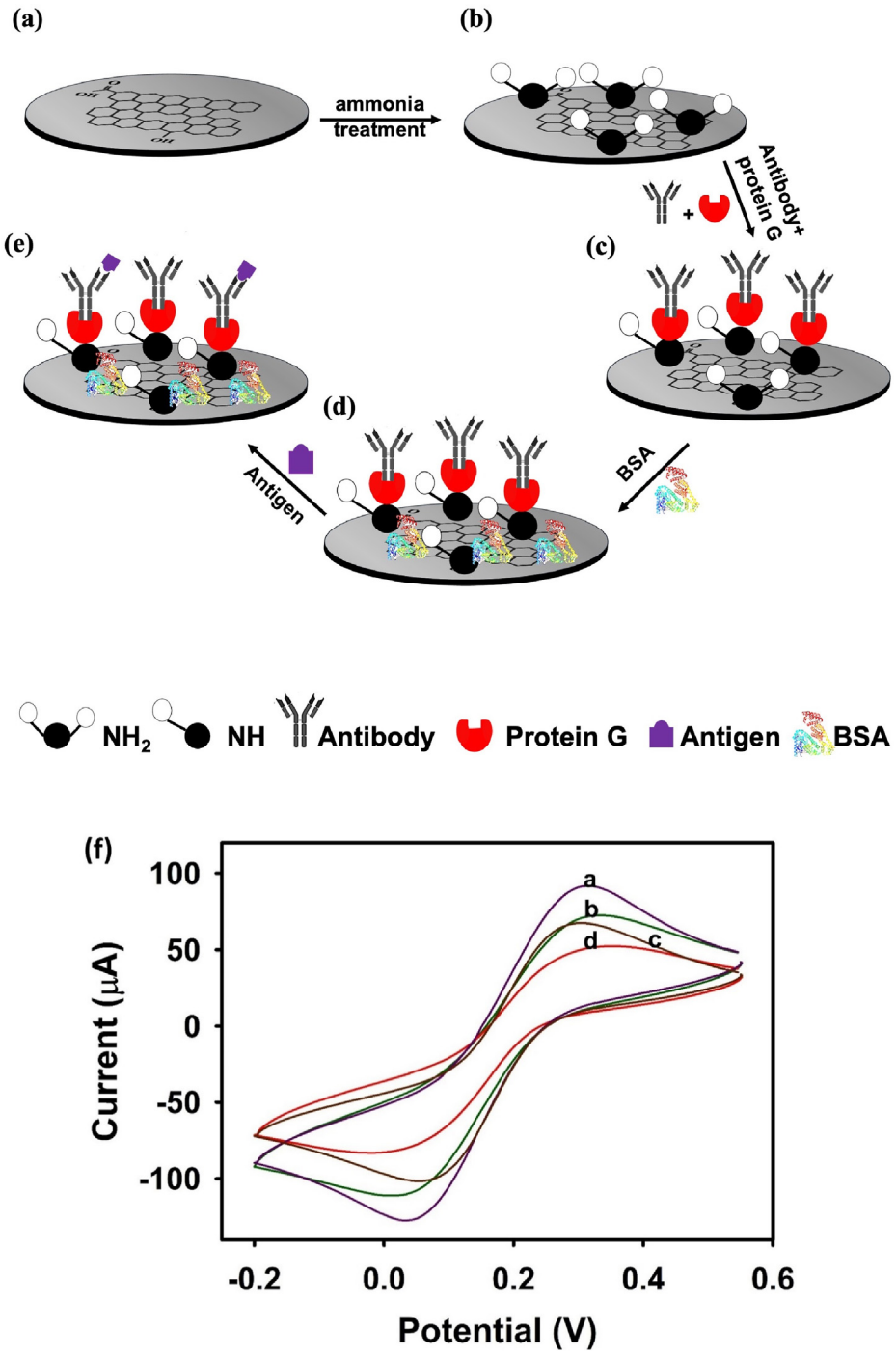

Fig. 3. Schematic representation of the fabrication process: (a) rGO working electrode, (b) modification with amines; (c) incubation with antibody and protein G mixture; (d) blocking with BSA; (e) detection of antigen and (f) voltammograms depicting each surface functionalization step (a–d) in 1 M PBS with 10 mM $[Fe(CN)_6]^{3-}$ and 1 M KCl solution at the scan rate of 0.05 mV s^{-1}. (A colour version of this figure can be viewed online.)

Case 2. NH_2/ oxygen functionalities: This is another possible mechanism for functionalization of rGO. The highly electronegative oxygen atoms present in epoxide (C–*O*–C), carboxyl (O–C=O) and hydroxyl (O–H) groups in rGO attract the H atoms from NH_3/NH_4^+ when immersed in the ammonia solution. In case of epoxide, NH_2 and H atoms get chemisorbed on the C and O atoms respectively, resulting in the formation of C–OH and C–NH_2(Fig. 2). The newly formed O–H groups interact with NH_2 via hydrogen bonding (OH···N) and lead to better chemisorption of NH_2 on rGO [31]. In case of carboxyl and hydroxyl groups, there is a formation O= C–NH_2 and C–NH_2 respectively along with the formation H–*O*–H [31,32]. Due to reduced number of functionalities in rGO and absence of high temperature [52], this mechanism is less likely than Case 1. Besides this, there is also a chance of physisorption of NH_3 on the surface of rGO. However, these interactions are quite weak [32,50,53].

Because each SPE consists of numerous rGO flakes, there are many NH_2 groups attached on the surface. These groups provide

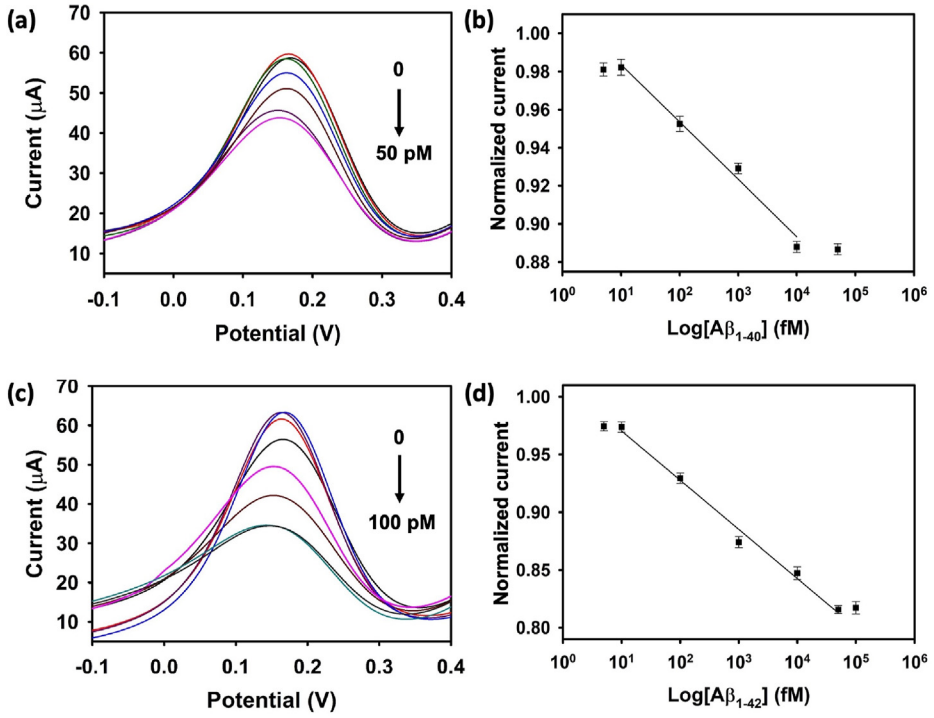

Fig. 4. Analytical performance of the biosensor (a) DPV curves obtained as a function of different concentration of $A\beta_{1\text{-}40}$ from 0 to 50 pM (0, 5, 10, 100, 1000, 10,000, 50,000 fM); (b) calibration plot for $A\beta_{1\text{-}40}$ for normalized current vs concentration on a logarithmic scale (n = 3); (c) DPV curves as a function of different concentration of $A\beta_{1\text{-}42}$ from 0 to 100 pM (0, 5, 10, 100, 1000, 10,000, 50,000, 100,000 fM)); (d) calibration plot for $A\beta_{1\text{-}42}$ for normalized current vs concentration on a logarithmic scale (n = 3). (A colour version of this figure can be viewed online.)

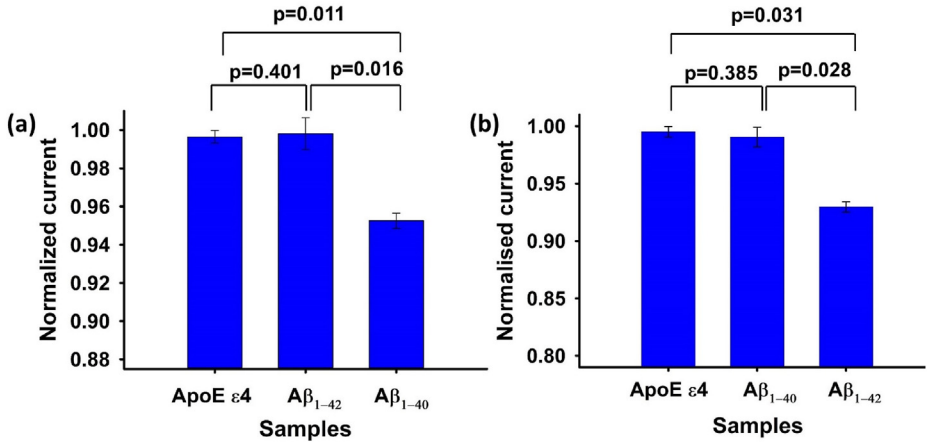

Fig. 5. Specificity of the biosensor for the detection of 100 fM of $A\beta_{1\text{-}40}$ (a) and $A\beta_{1\text{-}42}$ (b) as compared to interfering agents at 1 nM concentration ($p < 0.05$). (A colour version of this figure can be viewed online.)

large number of binding sites for antibody, which improves the overall sensitivity of the biosensor.

3.4. Electrochemical analysis

Electrochemical analysis of SPEs were performed using CV to understand the effect of various surface functionalization on the rGO surface. It provides information on the interfacial properties of attached layers based on charge transfer kinetics of the redox probe $[Fe(CN)_6]^{3-/4-}$ to SPE [10]. Schematic of the functionalization steps involved in the preparation of biosensor are shown in Fig. 3(a–e). The corresponding voltammograms for bare (purple), NH_2 (green), antibody (brown) and BSA (red) functionalized rGO SPE are shown in Fig. 3 (f). Chemisorption of NH_2 on rGO decreases the anodic peak current (I_{pa}) or the positive peak current from 91.969 μA to 72.25 μA. This is attributed to the increased electron transfer resistance due to the acquirement of the available electroactive sites on rGO by NH_2 groups. Immobilization of antibody and protein G mixture decreases the current further to 67.646 μA. This is due to the blocking of modified area from electrolyte/redox probe which affects the charge transfer [54]. Lastly, the attachment of BSA decreases the current to 50.594 μA as it binds to free functional groups on the surface to prevent the probability of non-specific binding [55]. Cathodic peak currents (I_{pc}) or the negative peak current showed a similar trend after each surface modification step.

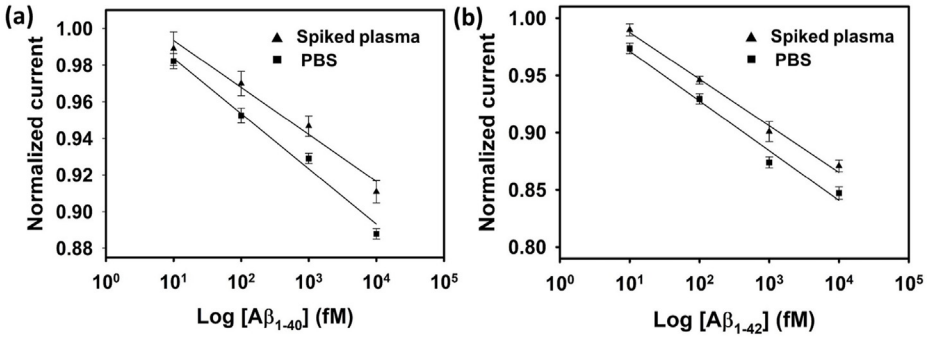

Fig. 6. Calibration plot depicting the linear responses in PBS and human plasma for (a) $A\beta_{1\text{-}40}$ and (b) $A\beta_{1\text{-}42}$.

3.5. Analytical performance of the biosensor

DPV was used to evaluate sensitivity of the biosensor against a wide range of Aβ concentrations. Fig. 4 (a, c) shows the output current as a function of various $A\beta_{1\text{-}40}$ and $A\beta_{1\text{-}42}$ concentrations. Calibration plot for the log of concentrations (in fM) versus normalized current is shown in Fig. 4 (b, d). Normalized current (I_C/I_{blank}) reduced linearly ($R^2 = 0.98$) with increment in the concentration of both biomarkers. The saturation was obtained after 10 pM for $A\beta_{1\text{-}40}$ and 50 pM for $A\beta_{1\text{-}42}$ attributed to the lack of antibodies left on the surface to capture any more antigen. The biosensor exhibited excellent LOD of 9.51 fM for $A\beta_{1\text{-}40}$ and 8.65 fM for $A\beta_{1\text{-}42}$. This excellent performance is attributed to the chemisorption of NH_2 groups on the rGO surface, which provide large number of binding sites for antibody. A comparative study with unmodified rGO depicted poor immobilization of $A\beta_{1\text{-}42}$ antibodies and consequently poor sensing performance. No major shifts in current were observed up to 10 pM after which slight shifts were obtained, however, they were negligible to be considered (Fig. S5). Futhermore, use of pro G leads to an optimal orientation of antibodies on the surface, which improves their capture efficiency [56]. The carboxyl terminal of pro G binds to the Fc site of antibody thereby making antigen binding (Fab) regions available for the target biomarkers [57]. Each pro G has two carboxyl terminals and even if one terminal is engaged with the Fc region of antibody, the other one is free to bind to the amines on sensor surface generating strong amide bonds [58,59]. However, due to the absence of an activator [60], it is also likely that the antibody and protein G mixture was immobilized on the surface through hydrophobic and/or electrostatic interactions. To the best of our knowledge, this is the lowest reported LOD with a label-free graphene biosensor (Supplementary information, Table S2).

3.6. Specificity studies

The specificity of biosensor towards $A\beta_{1\text{-}40}$ and $A\beta_{1\text{-}42}$ was evaluated with DPV measurements. The respective biosensors were incubated in 1 nM of interfering agents and 100 fM of target protein under similar experimental conditions. Fig. 5 (a,b) shows the bar graphs obtained from the normalized peak current values (to blank). Paired *t*-test was performed to check the significance of the data. The target protein shows a significantly lower response than the interfering species ($p < 0.05$). This confirms the high specificity of the biosensor towards the target biomarkers.

3.7. Spiked plasma analysis

The human plasma was spiked with known concentrations (in linear range of biosensor) including 10, 100, 1000 and 10,000 fM for $A\beta_{1\text{-}40}$ and $A\beta_{1\text{-}42}$. Normalized current vs log of concentration (fM) for each biomarker is shown in Fig. 6 (a, b) to show the applicability in biofluids. The calibration plot obtained in PBS was replotted here to show a comparison with the plasma results. The platform showed a similar linear relationship in the two matrices ($R^2 = 0.98$) for $A\beta_{1\text{-}40}$ and slightly higher ($R^2 = 0.99$) for $A\beta_{1\text{-}42}$. The detection sensitivity was obtained by dividing the slope of calibration plot with area of the electrode (normalized current/concentration (fM)/area (cm^2)) [61]. The value of sensitivity for $A\beta_{1\text{-}40}$ was obtained as 0.1032 in PBS and 0.0873 in plasma. The slight decrease can be attributed to the matrix effects of plasma. Similarly, the value of sensitivity for $A\beta_{1\text{-}42}$ was calculated to be 0.1508 in PBS and 0.1349 in plasma.

4. Conclusion

In summary, a novel functionalization technique for attaching NH_2 linker has been developed for the surface modification of rGO SPEs. It occurs through chemisorption of NH_2 groups predominantly on the edge and defects sites of rGO without damaging its structure, as confirmed by XPS, Raman and FTIR analysis. The functionalized electrodes were used for detection of $A\beta_{1\text{-}40}$ and $A\beta_{1\text{-}42}$ biomarkers. The NH_2 linker provides large number of binding sites for antibodies, which considerably enhances the sensitivity of biosensor. This results in an excellent LOD of 9.51 fM for $A\beta_{1\text{-}40}$ and 8.65 fM for $A\beta_{1\text{-}42}$, which are much lower than those reported elsewhere and good specificity for the target proteins. It was successfully validated with spiked human plasma. Extensive studies with clinical samples are still needed to verify the performance of biosensor in body fluids for clinical applications. Despite this, the proposed functionalization technique provides a simple and a cost- and time-effective approach for enhancing the sensitivity of graphene-based biosensors without the use of signal enhancers or labels.

CRediT authorship contribution statement

Jagriti Sethi: Conceptualization, Methodology, Investigation, Fabrication, Validation, Formal analysis, Writing – original draft. **Ahmed Suhail:** Methodology, Writing – review & editing. **Mina Safarzadeh:** Methodology, Writing – review & editing. **Anas Sattar:** Methodology, Writing – review & editing. **Yinghui Wei:** Supervision, Writing – review & editing. **Genhua Pan:** Supervision, Writing – review & editing, Project administration, Funding acquisition.

Declaration of competing interest

The authors declare that they have no known competing financial interests or personal relationships that could have appeared to influence the work reported in this paper.

Acknowledgements

This work is financially supported by the H2020 MSCA-ITN-ETN BBDiag project under grant No. 721281. We acknowledge the support of the Plymouth electron microscopy centre (PEMC) for performing scanning electron microscopy and Harwellxps for performing X-ray photoelectron spectroscopy.

Appendix A. Supplementary data

Supplementary data to this article can be found online at https://doi.org/10.1016/j.carbon.2021.04.074.

References

[1] Z. Liu, Z. Ma, Fabrication of an ultrasensitive electrochemical immunosensor for CEA based on conducting long-chain polythiols, Biosens. Bioelectron. 46 (2013) 1–7.
[2] R. Wang, et al., Ultrasensitive detection of carcinoembryonic antigen by a simple label-free immunosensor, Sensor. Actuator. B Chem. 176 (2013) 1044–1050.
[3] H. Su, S. Li, K. Kerman, Novel thiolated-PEG linker molecule for biosensor development on gold surfaces, Biosens. Bioelectron. 141 (2019) 111477.
[4] M. Gutiérrez-Capitán, A. Baldi, C. Fernández-Sánchez, Electrochemical paper-based biosensor devices for rapid detection of biomarkers, Sensors 20 (4) (2020) 967.
[5] D.R. Thévenot, et al., Electrochemical biosensors: recommended definitions and classification, Anal. Lett. 34 (5) (2001) 635–659.
[6] P. Carneiro, S. Morais, M.C. Pereira, Nanomaterials towards biosensing of Alzheimer's disease biomarkers, Nanomaterials 9 (12) (2019) 1663.
[7] V. Georgakilas, et al., Functionalization of graphene: covalent and non-covalent approaches, derivatives and applications, Chem. Rev. 112 (11) (2012) 6156–6214.
[8] W. Yang, et al., Carbon nanomaterials in biosensors: should you use nanotubes or graphene? Angew. Chem. Int. Ed. 49 (12) (2010) 2114–2138.
[9] B. Li, et al., Graphene electrode modified with electrochemically reduced graphene oxide for label-free DNA detection, Biosens. Bioelectron. 72 (2015) 313–319.
[10] J. Sethi, et al., A label-free biosensor based on graphene and reduced graphene oxide dual-layer for electrochemical determination of beta-amyloid biomarkers, Microchimica Acta 187 (5) (2020) 288.
[11] K.I. Bolotin, et al., Ultrahigh electron mobility in suspended graphene, Solid State Commun. 146 (9–10) (2008) 351–355.
[12] S. Taniselass, M.K.M. Arshad, S.C.B. Gopinath, Graphene-based electrochemical biosensors for monitoring noncommunicable disease biomarkers, Biosens. Bioelectron. 130 (2019) 276–292.
[13] B. Gadgil, P. Damlin, C. Kvarnström, Graphene vs. reduced graphene oxide: a comparative study of graphene-based nanoplatforms on electrochromic switching kinetics, Carbon 96 (2016) 377–381.
[14] D.-Y. Kang, et al., Ultra-sensitive immunosensor for β-amyloid (1–42) using scanning tunneling microscopy-based electrical detection, Biosens. Bioelectron. 24 (5) (2009) 1431–1436.
[15] M. Azimzadeh, et al., Early detection of Alzheimer's disease using a biosensor based on electrochemically-reduced graphene oxide and gold nanowires for the quantification of serum microRNA-137, RSC Adv. 7 (88) (2017) 55709–55719.
[16] S. Tonello, et al., Screen-printed biosensors for the early detection of biomarkers related to alzheimer disease: preliminary results, Procedia Engineering 168 (2016) 147–150.
[17] K. Settu, et al., Development of carbon–graphene-based aptamer biosensor for EN2 protein detection, Anal. Biochem. 534 (2017) 99–107.
[18] Z. Tehrani, et al., Generic epitaxial graphene biosensors for ultrasensitive detection of cancer risk biomarker, 2D Mater. 1 (2) (2014), 025004.
[19] M. Zhao, et al., Monolayer rubrene functionalized graphene-based electrochemiluminescence biosensor for serum cystatin C detection with immunorecognition-induced 3D DNA machine, Biosens. Bioelectron. 127 (2019) 126–134.
[20] N. Ruecha, et al., Label-free paper-based electrochemical impedance immunosensor for human interferon gamma detection, Sensor. Actuator. B Chem. 279 (2019) 298–304.
[21] A. Panchaud, et al., ANIBAL, stable isotope-based quantitative proteomics by aniline and benzoic acid labeling of amino and carboxylic groups, Molecular & Cellular Proteomics 7 (4) (2008) 800.
[22] A. Suhail, et al., Improved efficiency of graphene/Si Schottky junction solar cell based on back contact structure and DUV treatment, Carbon 129 (2018) 520–526.
[23] K. Islam, A. Suhail, G. Pan, A label-free and ultrasensitive immunosensor for detection of human chorionic gonadotrophin based on graphene FETs, Biosensors 7 (3) (2017) 27.
[24] O. Hanon, et al., Plasma amyloid levels within the Alzheimer's process and correlations with central biomarkers, Alzheimer's Dementia 14 (7) (2018) 858–868.
[25] T.-B. Chen, et al., Plasma Aβ42 and total tau predict cognitive decline in amnestic mild cognitive impairment, Sci. Rep. 9 (1) (2019) 13984.
[26] T. Wang, et al., Ultrasensitive microfluidic solid-phase ELISA using an actuatable microwell-patterned PDMS chip, Lab Chip 13 (21) (2013) 4190–4197.
[27] T. Kawata, et al., Improved sensitivity of a graphene FET biosensor using porphyrin linkers, Jpn. J. Appl. Phys. 57 (6) (2018), 065103.
[28] L. Lai, et al., One-step synthesis of NH2-graphene from in situ graphene-oxide reduction and its improved electrochemical properties, Carbon 49 (10) (2011) 3250–3257.
[29] M.A. Ali, et al., Lipid–lipid interactions in aminated reduced graphene oxide interface for biosensing application, Langmuir 30 (14) (2014) 4192–4201.
[30] M. Baraket, et al., Aminated graphene for DNA attachment produced via plasma functionalization, Appl. Phys. Lett. 100 (23) (2012) 233123.
[31] S. Tang, Z. Cao, Adsorption and dissociation of ammonia on graphene oxides: a first-principles study, J. Phys. Chem. C 116 (15) (2012) 8778–8791.
[32] E.C. Mattson, et al., Exploring adsorption and reactivity of NH3 on reduced graphene oxide, J. Phys. Chem. C 117 (20) (2013) 10698–10707.
[33] L. Rivera, et al., Reduction and Simultaneous Doping of Graphene Oxide to Repel LDL in Treatment of Atherosclerosis Disease, 2019 arXiv preprint arXiv: 1902.01850.
[34] C. Petit, M. Seredych, T.J. Bandosz, Revisiting the chemistry of graphite oxides and its effect on ammonia adsorption, J. Mater. Chem. 19 (48) (2009) 9176–9185.
[35] Z. Xing, et al., One-pot hydrothermal synthesis of Nitrogen-doped graphene as high-performance anode materials for lithium ion batteries, Sci. Rep. 6 (1) (2016) 26146.
[36] E.I. Bîru, et al., Advanced polybenzoxazine structures based on modified reduced graphene oxide, Polymers 10 (9) (2018) 941.
[37] T.W. Scharf, et al., Structural and tribological characterization of protective amorphous diamond-like carbon and amorphous CNx overcoats for next generation hard disks, J. Appl. Phys. 85 (6) (1999) 3142–3154.
[38] J. Nimita Jebaranjitham, et al., Fabrication of amine functionalized graphene oxide – AgNPs nanocomposite with improved dispersibility for reduction of 4-nitrophenol, Compos. B Eng. 171 (2019) 302–309.
[39] G. Sobon, et al., Graphene oxide vs. reduced graphene oxide as saturable absorbers for Er-doped passively mode-locked fiber laser, Opt Express 20 (17) (2012) 19463–19473.
[40] J. Shi, et al., Co3O4 porous nanorod/N-doped reduced graphene oxide composite with fast pseudocapacitive lithium storage for high-performance lithium-ion capacitors, J. Mater. Sci. 56 (12) (2021) 7520–7532.
[41] Z. Su, et al., Simultaneous reduction and surface functionalization of graphene oxide with wrinkled structure by diethylenetriamine (DETA) and their reinforcing effects in the flexible poly (2-ethylhexyl acrylate)(P2EHA) films, Compos. Appl. Sci. Manuf. 84 (2016) 64–75.
[42] C.-M. Chen, et al., Hierarchically aminated graphene honeycombs for electrochemical capacitive energy storage, J. Mater. Chem. 22 (28) (2012) 14076–14084.
[43] A.C. Ferrari, et al., Raman spectrum of graphene and graphene layers, Phys. Rev. Lett. 97 (18) (2006) 187401.
[44] H. Abdali, A. Ajji, Preparation of electrospun nanocomposite nanofibers of polyaniline/poly(methyl methacrylate) with amino-functionalized graphene, Polymers 9 (9) (2017).
[45] B. Wang, et al., Chemical amination of graphene oxides and their extraordinary properties in the detection of lead ions, Nanoscale 3 (12) (2011) 5059–5066.
[46] Z. Su, et al., Simultaneous reduction and surface functionalization of graphene oxide with wrinkled structure by diethylenetriamine (DETA) and their reinforcing effects in the flexible poly(2-ethylhexyl acrylate) (P2EHA) films, Compos. Appl. Sci. Manuf. 84 (2016) 64–75.
[47] F.H. Baldovino, et al., Synthesis and characterization of nitrogen-functionalized graphene oxide in high-temperature and high-pressure ammonia, RSC Adv. 6 (115) (2016) 113924–113932.
[48] A. Jorio, et al., Measuring Disorder in Graphene with Raman Spectroscopy, 2011.
[49] P. Veluswamy, et al., Sono-synthesis approach of reduced graphene oxide for ammonia vapour detection at room temperature, Ultrason. Sonochem. 48 (2018) 555–566.
[50] R. Kumar, et al., Room temperature ammonia gas sensor using ester functionalization of graphene oxide, Mater. Res. Express 6 (9) (2019), 095618.
[51] S. Banerjee, T. Hemraj-Benny, S.S. Wong, Covalent surface chemistry of single-walled carbon nanotubes, Adv. Mater. 17 (1) (2005) 17–29.
[52] S.S. Shazali, et al., Facile hydrothermal method for synthesizing nitrogen-doped graphene nanoplatelets using aqueous ammonia: dispersion, stability in solvents and thermophysical performances, Mater. Res. Express 5 (3) (2018), 035042.
[53] C.C. Kiang, P. Martin, Chemically modified graphenes as detectors in lab-on-chip device, Electroanalysis 25 (4) (2013) 945–950.
[54] A. Baradoke, et al., Properties of Anti-CA125 antibody layers on screen-printed carbon electrodes modified by gold and platinum nanostructures, Electrochim. Acta 306 (2019) 299–306.
[55] K. Islam, et al., Development of a label-free immunosensor for Clusterin detection as an Alzheimer's biomarker, Sensors 18 (1) (2018) 308.

[56] Y. Yang, Y. Huang, C. Li, A reusable electrochemical sensor for one-step biosensing in complex media using triplex-forming oligonucleotide coupled DNA nanostructure, Anal. Chim. Acta 1055 (2019) 90–97.
[57] N.G. Welch, et al., Orientation and characterization of immobilized antibodies for improved immunoassays (Review), Biointerphases 12 (2) (2017), 02d301.
[58] U. Sjöbring, L. Björck, W. Kastern, Streptococcal protein G. Gene structure and protein binding properties, J. Biol. Chem. 266 (1) (1991) 399–405.
[59] Y.-S. Sohn, Y.K. Lee, Site-directed immobilization of antibody using EDC-NHS-activated protein A on a bimetallic-based surface plasmon resonance chip, J. Biomed. Opt. 19 (5) (2014), 051209.
[60] D. Kim, A.E. Herr, Protein immobilization techniques for microfluidic assays, Biomicrofluidics 7 (4) (2013), 041501.
[61] N. Zakaria, et al., An impedimetric micro-immunosensing assay to detect Alzheimer's disease biomarker: aβ40, Anal. Biochem. 555 (2018) 12–21.
[62] Suhail A., et al., Label-free electrochemical biosensor for the detection of bodyfluid based biomarkers, patent application number: EP20217463.7.